Combined effects of nanosecond laser-induced surface oxidation and nanostructure formation for selective colorization of nickel surfaces

Huazhong Zhu[1,2] · Martin Ehrhardt[1] · Pierre Lorenz[1] · Joachim Zajadacz[1] · Jian Lu[2] · Klaus Zimmer[1]

Abstract

Metal surfaces can be nanostructured by laser irradiation making use of different effects ranging from thin film generation to nanostructures formation. Here, the colorization of pure nickel surfaces by nanosecond laser irradiation in air is demonstrated and studied in detail. Correlations between chromaticity coordinates and laser-processing parameter show that the accumulated fluence is the dominating factor in creation of a specific colored surface. The color of the laser-irradiated surfaces shows both angle-dependent and angle-independent in reliance on the processing conditions. The examination of the laser-colored surface demonstrates that lateral and vertical organized, laser-induced structures with nano-, micro-, and mesoscopic scales can be found simultaneously which contribute to the colorization in a particular manner. A comprehensive analysis of the processes involved in the color formation at nickel was performed by examining the surfaces by SEM, reflectometry, XPS, and XRD to verify the multi-process mechanisms of color formation. The most saturated colors result from interference effects within the redeposited layers. It was found that controlling the hatching distance applying optimized laser fluence enables a wider color range and allows a very precise setting of the color. Based on the extracted laser-processing parameters, the surface coloration of arbitrary pattern with desired optical properties becomes practicable, and nanosecond laser color marking can, therefore, be expanded to potentially new applications.

1 Introduction

Colorizing on commercial metal surface is usually applied in the area of aesthetic decoration or reliable marking to replace the natural color of metals. In the past, this kind of processing is typically performed by techniques of painting (printing), emulsion coating, and electrolytic anodizing. Recently, laser-induced colorization, which is generally known as laser color marking, has been attract a lot of attention in scientific community due to the potential industrial applications that can be realized by the high processing speed, the high local resolution, the options for color control, and opportunities for automation [1–8].

According to the former results, this laser-based colorization technique of metals can comprise different color formation processes such as periodic surface grating diffraction, thin film interference, and nanoparticle-induced surface plasmon resonance [4–6, 9]. In experiments with nanosecond fiber laser [7, 9] or solid-state lasers (for instance Nd:YAG laser [3]), the achieved surface color can usually be attributed to oxides films [1, 9]. The color spectrum in the visible range is a result of thin-film interference (interference color) and is determined by the oxide thickness, the refractive index including the absorption, the altitudinal angle of light incidence, and the order of interference [10, 11]. Other laser-induced color effects related to periodic micro/nanostructure of surfaces (structural color; i.e., color changes with viewing angle and incident angle of illumination light). Several kinds of micro/nanostructures including particles are usually achieved by ultrashort laser processing [12–15]. This optical diffraction effect of periodic structures is commonly attributed to the formation of laser-induced of periodic surface structures (LIPSS) [16, 17]; linear LIPSS sometimes called "laser-induced ripples". A further contribution to color formation at surfaces can result

✉ Klaus Zimmer
  klaus.zimmer@iom-leipzig.de

[1] Leibniz Institute of Surface Engineering (IOM), Leipzig, Germany

[2] Department of Applied Physics, Nanjing University of Science and Technology, Nanjing 210094, People's Republic of China

from plasmonic effects which also belongs to nanostructures that emerge from wavelength- and size-dependent resonant interactions between illuminating light and nanoparticles (NPs) or nanostructures [18]. Such optical active nanostructures can be found at surfaces or can be incorporated in thin transparent films. Laser ablation processes can result in the formation various nanostructures by a diversity of processes [6, 8]. In the case of the appearance of localized surface plasmon resonance (LSPR; plasmonic color), the optical properties of the nanomaterials are usually different from the bulk [19–21]. Often, ultrashort-pulsed laser (femto- and picosecond laser) are more applicable to accomplish the formation of structural color by LIPSS or LSPR. At high densities of the near-surface nanostructures, low reflectivity can be achieved across the whole visible spectrum [22]. Here, the multiple scattering at the nanostructures contributes to the dark surface in a large extend [23].

Nanosecond fiber laser with high flexibility, fast processing speed, and low operating costs is at present a commonly used tool for industrial color laser marking. However, in nanosecond scale (especially in 100 s ns), remarkable thermal effects induced by laser irradiation becomes the barriers for LIPSS formation, which consequently makes the colorization results mainly from oxide growth on the metals [5, 24]. Obviously, versatile color effects can be achieved if different colorization mechanisms can be combined within one marking process.

This study aims to investigate the color marking of nickel by the utilization of different mechanisms of the color formation under sub-nanosecond laser irradiation. In particular, the combination of nanostructure-related and thin-film-induced coloring processes provides extended set of color patterns and color appearance, including azimuthal-independent color and structural colors. In addition, the precise control of color formation on commercial nickel surfaces by a scanning strategy is shown enabling a high repeatability and stability of coloring process, which is the key issue for the industrial application of this technology.

2 Experimental setup

The work was performed using a pulsed ytterbium-doped fiber laser source (PyroFlex from PyroPhotonics Lasers Inc.) for irradiating nickel with thickness of 0.2 mm (electroplated, polished nickel sheet) and 1 mm (frosted nickel sheet) at a wavelength of 1064 nm. Before laser treatment, the nickel samples were pre-cleaned in an ultrasonic bath with ethanol for 20 min. The laser parameters pulse duration (1 ns) and repetition rate (10 kHz) were kept constant in the experiments. The applied laser fluence F_0 was varied from 2.0 to 10.0 J/cm^2. All experiments were carried out in air with a relative humidity of 45% and room temperature

(21 °C). The laser beam with polarization orientation (P) along the scanning direction was scanned by built-in galvo scanner. The laser beam was focused to the sample surface through an F-Theta lens ($f = 160$ mm, working area is 100×100 mm). The diameter of the Gaussian beam spot was obtained to be 35 ± 1.2 µm at the focal position.

Line-by-line laser scanning (Fig. 1a) was applied as colorization strategy. The scanning overlap (SOVL), i.e., the overlap of successive laser spots during scanning, was set at 0% by fixing the scanning speed to 350 mm/s and neglecting the fluence dependence of the laser crater size. The hatching overlap (HOVL), i.e., the ratio of spot distance of subsequent scan lines, was changed by adjusting the hatching distance from 0.5 to 8 µm with a step of 0.5 µm. Using different combinations of hatch distance and laser fluence, a colorized matrix was established to give a quick retrieval on achievable colors.

A color-reading platform (Fig. 1b), which consists of digital camera and D65 illumination light, was set up for an objective evaluation of the color characteristics depending on the azimuthal (β) and altitudinal (α) angle in relation to the laser-processing parameters. Reference images were acquired from a standardized reference color palette with the same setup to normalize the sample colors to reference standard. The colorimetric data can be used for characterizing the colorization capacity and can be used to give evidence to the reasons for the achieved colors.

The surface morphology of colorized regions after laser treatment was examined by optical microscope (OM) and scanning electron microscope (SEM). In addition, the phase structure and the chemical composition were evaluated using X-ray photoelectron spectroscopy (XPS) and X-ray diffraction (XRD).

3 Experimental results and discussion

Mainly parameter combinations of pulse energy, scanning speed, and hatching distance were screened in relation to the particular color characteristics of laser-irradiated nickel. First, the ablation threshold of nickel was determined to be 1.45 ± 0.05 J/cm^2 for polished sample and 1.33 ± 0.06 J/cm^2 for frosted sample.

3.1 Accumulated fluence-dependent effect of coloration control

The concept of accumulated fluence was used to study the scanning strategy to represent the total laser dose on a specific irradiated area. With this index, the two independent processing parameters, laser fluence and hatching distance, can be combined to implement for controllable color formation.
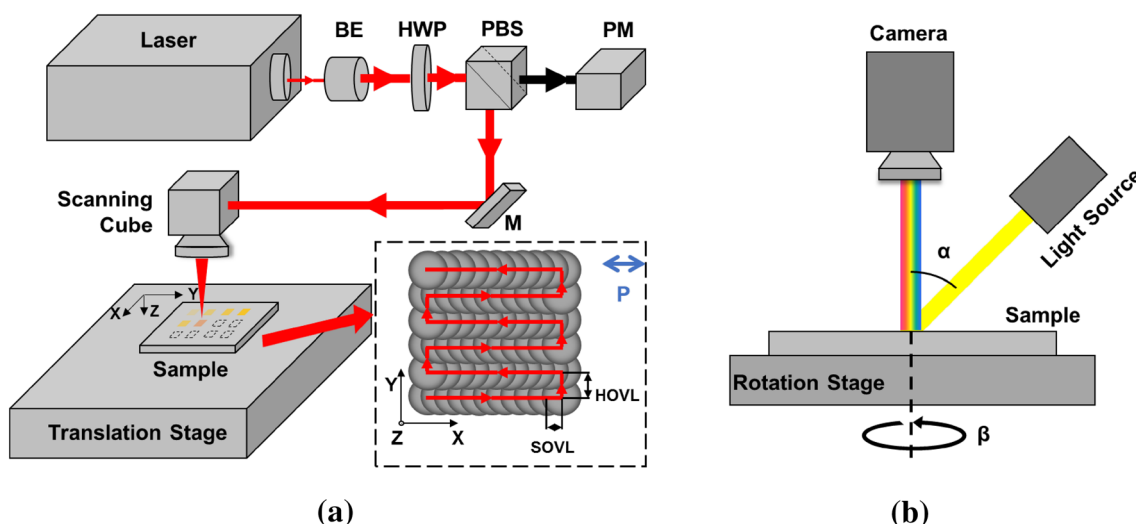
Fig. 1 Sketches of the experiments for laser-induced colorization and color reading: **a** schematic diagram of the laser-processing setup: *BE* beam expander, *HWP* half-wavelength plate, *PBS* polarizing beam splitter, *M1* and *M2* mirrors, *PM* power meter, scanning cube: galvanometer scanner and F-Theta lens. The inset represents the layout of the laser-scanning strategy. Furthermore, the polarization P of the laser is depicted. **b** Schematic illustration of detection geometry (illumination–observation) for color evaluation. The camera is perpendicular to the sample surface, and the altitudinal angle α and azimuthal angle β can be adjusted both

Since the SOVL is fixed to be zero, the pulse distance along *X*-axis has been omitted, and the accumulated fluence is determined by

$$F_{acc} = \frac{2\sqrt{2}E}{\pi\omega_0 L},$$ (1)

where E is laser pulse energy, ω_0 is the laser spot radius (Gaussian), and L is hatching distance [9]. Despite SOVL is fixed, the diameter of ablation regions in the experiments is not identical, but depends on the actual applied laser fluence according to the Gaussian intensity distribution.

Figures 2 and 3a show the coloration results on frosted and polished nickel at a same observation condition. The range of colors produced using different combinations of laser-processing parameters can be seen. In these experiments, the hatching distance is varied as columns from 0.5 to 7 µm with a step of 0.5 µm, whereas the laser fluence is changing within a row from 10 to 2 J/cm². No obvious color discrepancy on both types of nickel samples, except for the difference in saturation of several colors; the color obtained on frosted sample seems to be more vivid compared to that than obtained on polished one. On the other hand, structural colors mainly appear on polished nickel samples, as presented in Fig. 3b–d. Both observations may be related to the surface topography; in particular, frosted samples that feature some roughness / waviness with a higher angular distribution of the surface are expect to have an altered (increased) local light-incidence angle.
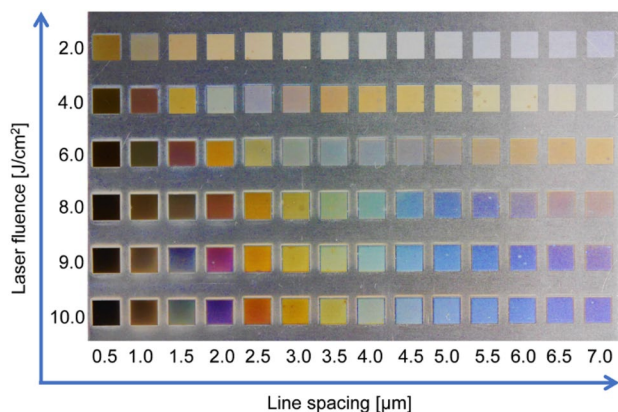

Fig. 2 Matrix of the color palette obtained on frosted nickel surface with different combinations of laser fluence and hatching distance. The size of each single marked field is 4×4 mm. Color reading and image taken is done at altitudinal angle α of 5° and azimuthal angle β of 0

To further show the correlation between specific color and accumulated fluence, the color performance is quantitatively evaluated using the HSV (Hue, Saturation, Value) color model which represents the human vision of colors in a more natural manner.

Figure 4a shows the plot of hues obtained with different accumulated fluences that calculated from the data of Fig. 2. The periodical change of hues with the increasing of accumulated fluence is demonstrated. Such cyclic reappearance of colors is typically a sign for interference effects, which is related to the oxide layer thickness.
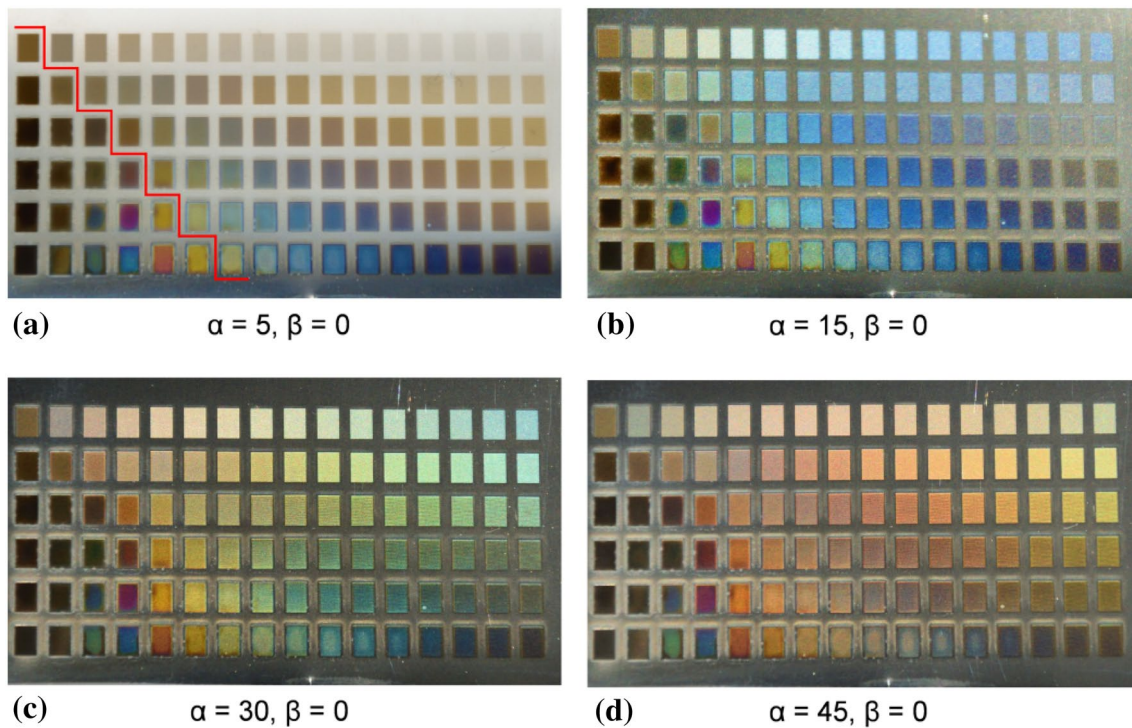
(a)   α = 5, β = 0   **(b)**   α = 15, β = 0

(c)   α = 30, β = 0   **(d)**   α = 45, β = 0

Fig. 3 Rectified, optical images of color palette achieved on polished nickel surface with the same laser parameter field, as shown in Fig. 2. Images were taken with different altitudinal angles of: **a** 5°, **b** 15°, **c** 30°, and **d** 45°. The parameter ranges are: laser fluence 2 to 10 J/cm² and line spacing 0.5–8 μ (according to Fig. 2). The size of each marked field is 3×4 mm

Fig. 4 HSV color space representation: **a** hue component (the color bar is shown on the right side of the graph) versus accumulated fluence calculated from data of Fig. 2, where the green, brown, pink, blue, red, and black symbols represent the data for laser fluences of 2–10 J/cm² in steps of 2 J/cm², respectively, **b** brightness values (V) for color obtained with accumulated fluence above 200 J/cm², triangle points represent colors in Zone IV, and square data points refer to darker color tone generated with fluence above 300 J/cm²
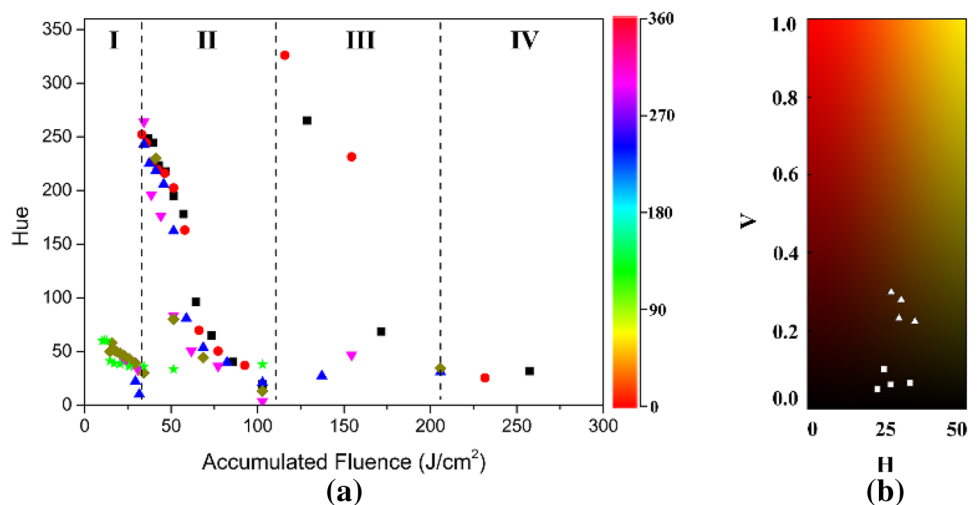
To clearly describe the distribution of hues, the accumulated fluence axis is divided into four sections. Zones I–III represent three consecutive color cycles (0–360 hue). In zone IV, however, a color cycle is not clearly seen, but only browns or ochres hue occur. As shown in Fig. 4b, the colors obtained in this region generally have low brightness values (V component in HSV), so that any color tends to be dark, which makes the color identification critical. Such darkening effects are known from ultrashort pulse laser processing of

metals and are related to the appearance of a nanostructured surface of an extended thickness [22]. Therefore, the utilization of doses above 200 J/cm² is not advised for applications.

As can be seen from Fig. 4a, zone III has a relatively large "color capacity", so a supplement analysis was carried out by extending the hue data in this region.

With further reducing of hatching distance step from 0.5 to 0.1 μm, colors obtained in the hatching distance range from 0.5 to 3 μm were enriched, as shown in Fig. 5a, and a
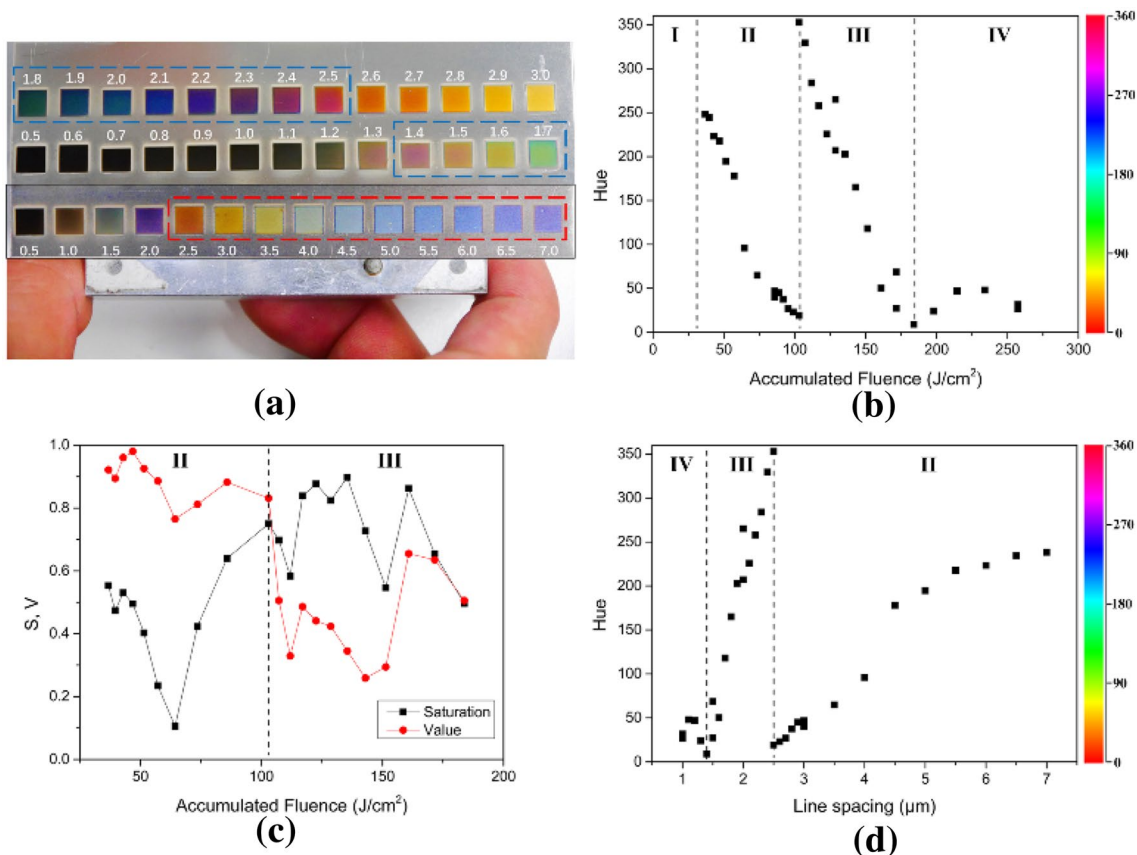
(a)

(b)

(c)

(d)

Fig. 5 Influence of hatching distance increment on color rendering (increment was reduced from 0.5 to 0.1 μm, $F_0 = 10$ J/cm^2): **a** photograph of the colorized sample, **b** diagram of the hue versus accumulated fluence, **c** diagram of saturation (S) and value (V) versus accu-

mulated fluence, **d** diagram of hue versus hatching distance. The red and blue boxes in **a** refer to colors achieved within the second- and third-order color cycles, respectively

more complete third-order color cycle (blue dashed boxes) is accordingly generated, as shown in Fig. 5b. In addition, inconspicuous colors (green, for instance) can also be obtained. Figure 5c further indicates that in addition to the wider color gamut, the third-order color cycle shows higher saturation (and lower color brightness) when compared to the second-order color cycle, which means that a better color performance can be expected in this zone.

Figure 5d shows the hue distribution over hatching distance for fixed laser fluence. Hence, the hatching distance becomes the only parameter for the determination of color formation. It can be seen that the third-order color cycle has a higher sensitivity (~ 315 deg/μm) to process parameter than that of second-order color cycle (~ 55 deg/μm), where the sensitivity can be evaluated by defining it as the gradient of hue distribution over hatching distance. The result implies that the second-order color cycle has a better fault tolerance and higher stability, and is, therefore, more recommendable for technical coloration applications that require reliable color formation and short-processing time. In contrast, high sensitivity of the third-order color cycle requires high

precision marking systems to meet the demands of color reproduction, but offers a wider color range.

3.2 Nanostructures for generation for angle-independent colorization

Several surface analysis techniques were applied to study the layer found after laser colorization. EDX studies show that the main components of the redeposited layer are Ni and O. XRD results show several peaks that can be assigned nickel (Ni) and crystallized nickel(II) oxide (NiO). With increasing the accumulated fluence, and consequently the appearance of coloring or darkening, the peak area of nickel compounds increases, suggesting a higher content of these components near the surface (see Fig. 6a). The reason should be related to the higher amount of ablated and redeposited material.

Further analysis by XPS reveals the mixed composition of the top surface and the appearance additional components that not forming a crystalline phase or only appears near the surface. In addition to O^{2-}, other anions, OH^-, NO_3^-, CO_3^{2-}, are identified from the XPS spectra (Fig. 6d),
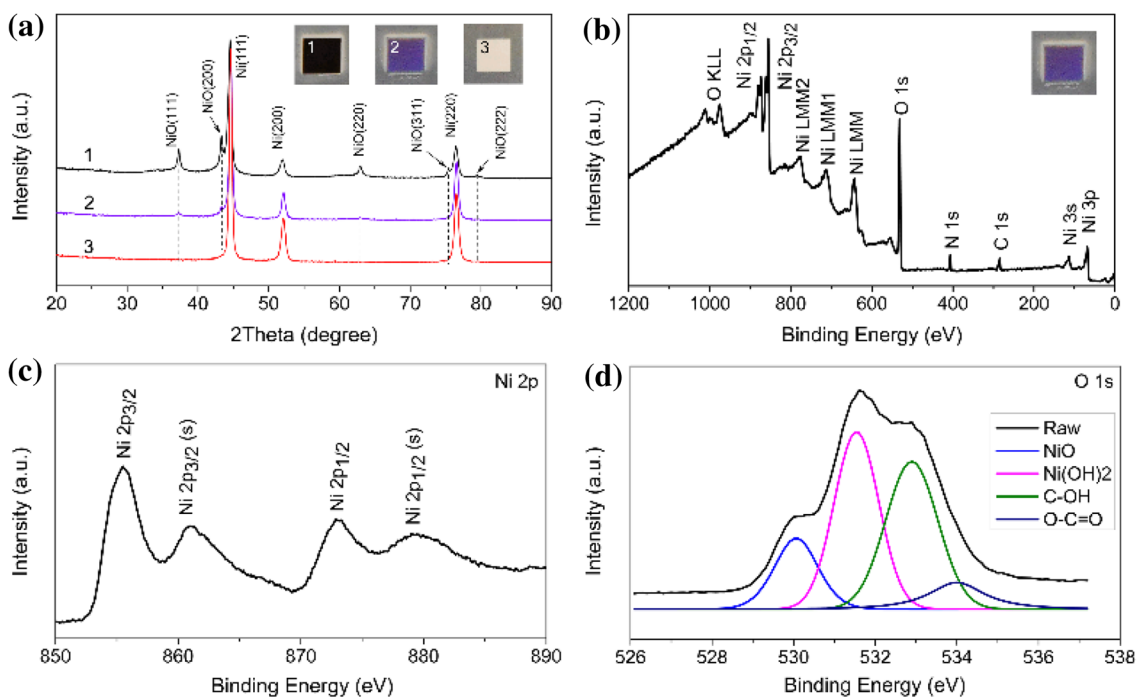
Fig. 6 Elemental analysis of irradiated surface: **a** XRD spectra of three colorized regions formed at hatching distance of 0.5, 2, and 8 μm, respectively, with laser fluence fixed at 10 J/cm², **b** survey XPS spectrum for colorized area (purple color) formed at hatching distance of 2 μm and laser fluence at 10 J/cm², **c** details of Ni 2p spectrum, **d** deconvolution of O 1 s spectrum

suggesting the appearance of different compounds. In particular, the content of OH⁻ probably from nickel(II) hydroxide changes considerably with the changing of the processing parameters; their amount decreases with increasing the accumulated fluence.

It is reasonable to assume that these extra compositions are probably come from the further reactions of NiO with air components (especially the moisture), or is directly created during the laser ablation in humid atmosphere [25]. Therefore, it seems simple to expect a two-layer structure with thin layer of $Ni(OH)_2$ on top of NiO. The contributions from the two layers to color formation are similar to the explanation for color formation of stainless steel or titanium [5].

Due to the fact of periodical reappearance of similar colors observed in the experiments (see Fig. 3) (oxide), film-related interference effects are believed to be the major reason for ablation-induced color formation which confirms the former work [7, 9, 26]. However, in addition to oxide film formation, other laser-induced processes including material ejection and nanoscale droplets deposition [27, 28] also have potential impacts on the final color appearance especially in the case of intense laser ablation [22]. Therefore, in addition to film formation, laser-induced nanostructures (nanoparticles) need to be considered for the discussion of the colorization mechanism.

Figure 7 shows the SEM images of the colorized samples, irradiated with different hatching distances at laser fluence of 10 J/cm². The surface topographic features including embedded nickel "NPs", cracks, and other nanostructures were observed. This "roughening" effect can gain the oxide formation process, since the porous-like surface structures and the "NPs" [29] provide a larger surface for air diffusing to the metal-surface-enhancing chemical reactions and reduce limitations due to the already formed oxide film. Furthermore, a clear correlation between size of nanostructures ("NPs") and hatching distance can be seen, which indicates that this parameter (or accumulated fluence) plays a key role in controlling of particle size.

From SEM images, the average size of NPs in each patch was determined using an image-processing software imageJ. As presented in Fig. 8, statistical results demonstrate a reduction of the average NP's size from ≈ 60 to ≈ 13 nm with increasing of hatching distance from 1 to 7 μm. With decreasing of accumulated fluence, the laser-treated surface appears smoother, finer, and more compact (shown as right part in Fig. 7e. Indeed, particle-like nanostructures on the surface disappear when the accumulated fluence is decreased to approximately 52 J/cm² Therefore, the impact of nanostructures for coloration is reduced for low laser dose values and the color is mainly determined by the thickness of nickel compound film.

For further analyzing the response of near-surface NPs to incident light, the optical resonance is calculated numerically based on Mie theory [30, 31]. In Fig. 9, the simulated

Fig. 7 SEM images of nano-structures formed on nickel surface after laser scanning with hatching distance of: **a** 1 μm, **b** 2 μm, **c** 3 μm, and **d** 4 μm, at fluence of 10 J/cm². The green, blue, red, and yellow arrows refer to nanoparticle, nanoparticle clusters, cracks, and isolated large particles with size of several hundred nanometers. **e** Comparison of nanostructured surface obtained with hatching distance of 2 μm (left) and 4 μm (right)
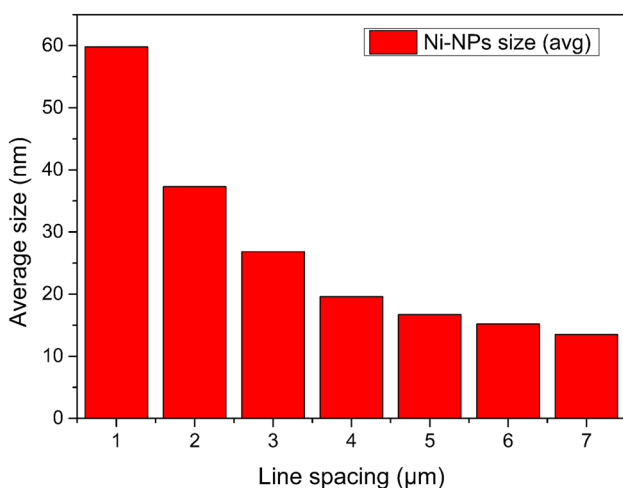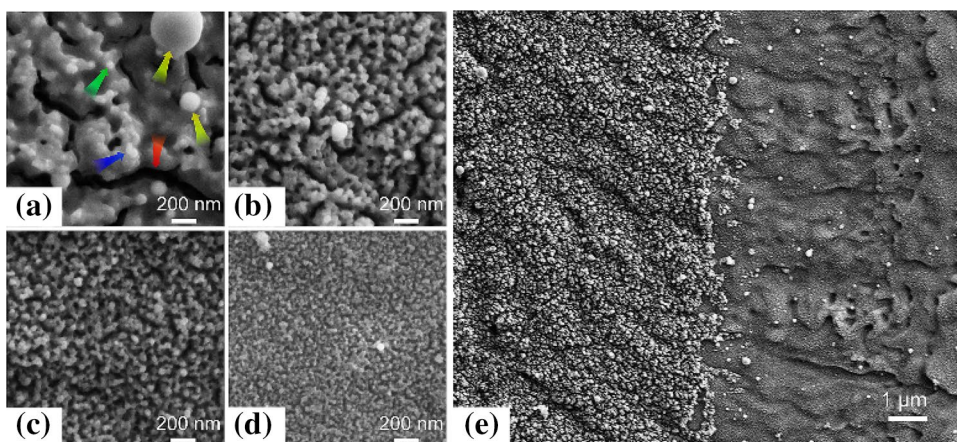

Fig. 8 Average size of nickel particle of a colored surface in dependence on the hatching distance
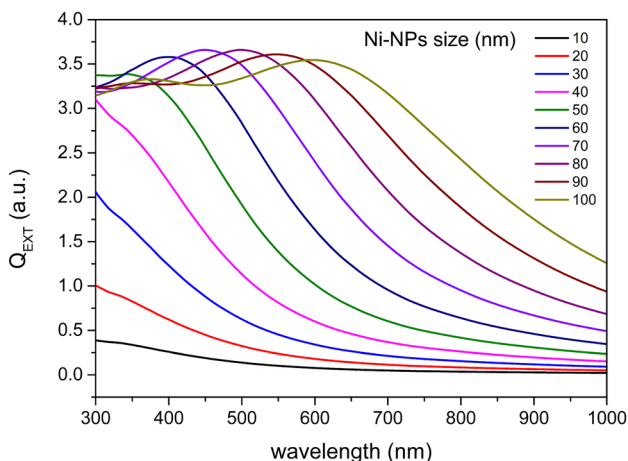

Fig. 9 Extinction efficiency from Mie theory for nickel NPs with different sizes. The dielectric constants are taken from Palik [32]

results of the resonance frequency for nickel NPs with different particle sizes is shown. A red-shift of the resonant wavelength for larger NPs size is observed especially for the size range from 50 to 100 nm. On the other hand, for the NPs smaller than 40 nm, the influence of NPs resonance effect to the visible spectrum is no longer that important. According to the relationship between average NPs' size and hatching distance, as shown in Fig. 8, the NP influences are reduced for hatching distance above 2 μm. This can suggest that the color formation is determined mainly by the formed nickel compound film. In particular, for lower hatching distance effects of localized surface, plasmon resonance (LSPR) should be considered for color generation.

The particle size findings are in agreement with the result of colorimetric analysis, as discussed in Sect. 3.1, where dark, brown colors occur at high doses meaning small hatching distance distances of less than 1 μm. Here, the calculated red shift as well as the effect of absorption enhancement by multi-scattering in the porous colloid structures can help in explaining the observed colors and low brightness (as shown in Fig. 7a–b).

3.3 Ripple-like structure formation

The change of the color in dependence on the rotation (azimuthal) angle β was measured for selected samples. Figure 10 shows the dependence of the HSV model parameters in dependence from the rotation of the sample at a given altitudinal angle. The change of the color for different altitudinal angles is right hand side for an azimuthal angle of 200°.

A clear dependence of the colors, the brightness, and the saturation from the azimuthal angle can be seen. The rather slow varying values with the angle probably are related to the divergence of the illuminating white light source.

In general, this kind of color appearance is formed by different kinds of LIPSS (ripples) [12–16]. In the experiments, self-organized periodic subwavelength structure can
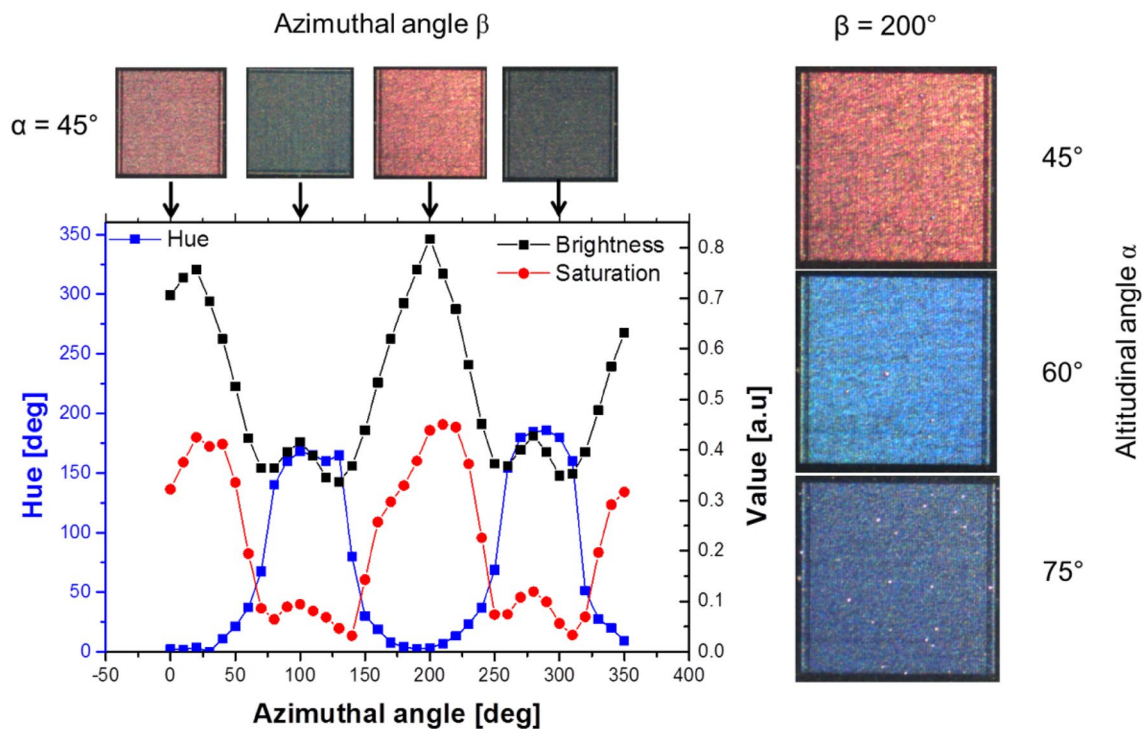
Fig. 10 Dependence of the HSV (Hue, Saturation, Value) color model parameter from the azimuthal angle. The selected area was treated with hatching distance of 5 μm at laser fluence of 2 J/cm². The color change with the altitudinal angle is shown for a rotation, azimuthal angle of 200°. Obviously, there is a slight misorientation of the ripples to the measurement angle

be found. In addition, patterns originating from the spot scanning can also be observed. The strength of both types of pattern depends on the HOVL and, therefore, on the applied laser dose. Due to the orientation of the structures, these can be considered as diffraction gratings. Hence, the resulting dispersive effect is more reasonable to be considered as the mechanism for angular-dependent color formation. Typical examples of surface morphology after laser treatment are shown in Fig. 11 for fluence of 10 J/cm² and hatching distance at 2 μm, 3 μm, 4 μm, and 7 μm; the corresponding accumulated fluences are 128–36 J/cm², respectively.

It can be noticed that for higher accumulated fluences (or smaller hatching distance), these regular surface microstructures will gradually fade away or disappear completely. The threshold for transition from angle-independent color to structural color appearance, which is around 85.8 J/cm² or at a hatching distance at 3 μm for 10 J/cm² (see Fig. 11b), also the critical point for LIPSS appearance was found.

In relation to the sequence of processes occurring during laser colorization, the mechanism is dominated by redeposition of ablated material and the formation of periodic pattern, e.g., LIPSS. In the sequence of processing, meaning with scanning the laser spot, first, most of the nanostructures including a potential oxide layer is removed due to ablation within the ablation spot ($F > F_{th}$). Outside the ablation spot, first ripples and resolidification rims generate surface pattern comprising LIPSS and the scanning strategy-dependent pattern. Thereafter, the still nearby happen laser ablation with the redeposition of debris, including NPs and modified substrate material (Ni), causing the formation of a cover layer. For smaller hatching distance, larger particle can be found pile up and forming such porous nanoparticle layer, which totally covers the surface microscale features, as shown in Fig. 7e (left part) and Fig. 11a. In contrast, smaller particles cover conformal surface patterns and have, due to the higher reactivity, the tendency of forming an oxide layer. In this case, the ripple-like structure is still remaining even with a thin compact oxide layer left atop, which can be seen in Fig. 7e (right part) and Fig. 11c.

In addition, Fig. 11d shows that for a too wide hatch distance (accumulated fluence unduly decreased), ripple-like structures are reduced, because they appear only near the spot edge. There, the laser fluence near the ablation threshold provides conditions for ripples formation, whereas in the center region of Gaussian laser spot melting for ns pulses occurs. Therefore, the effective area covered with ripples decreases with increasing the hatching distance.

Considering the simultaneously presence of surface oxide, nanoparticles, and ripple-like structure, which can be expected for a hatching distance over 3 μm, a general evaluation of the color formation ought to be taken. In this case, the observed color needs to be discussed on the coupling

Fig. 11 Optical microscope images of ripple-like structures obtained with pulse fluence of 10 J/cm^2 and hatching distance at: **a** 2 µm, **b** 3 µm, **c** 4 µm, **d** 7 µm
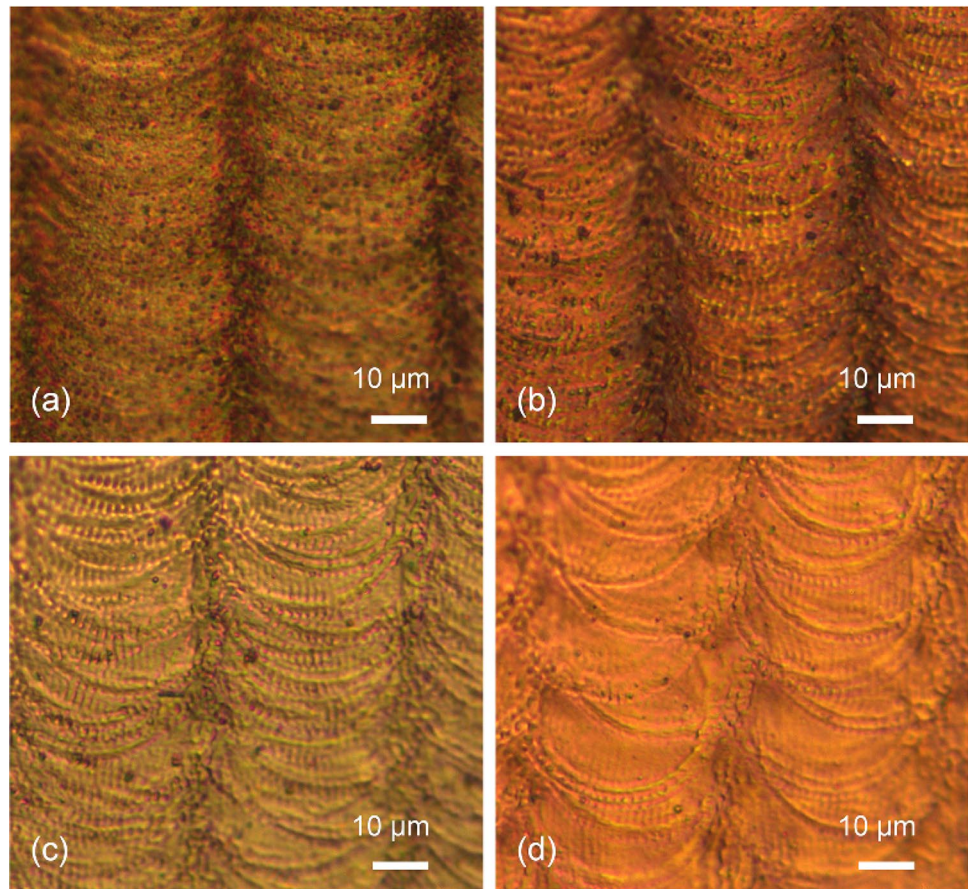
from both azimuthal angle-independent and angle-dependent effects resulting from a complex interplay between these various mechanisms. However, the specific contributions of each effect to the final color state are hard to analyze quantitatively due to the interdependency of each effect, which, therefore, needs further studies.

4 Conclusions

The controllable colorization of pure nickel surface via direct ablation in the air by ns fiber laser irradiation is presented. The analysis of the achieved color palettes indicates that each individual color is mainly determined by a corresponding accumulated fluence obtained from particular combinations of processing parameters. In contrast to former results, the selection of the accumulated fluence by adjusting the scanning hatching distance keeping constant the laser fluence seems favourable, as a wide spectral range can be achieved. Furthermore, both angle-dependent and angle-independent colors could be formed simultaneously that is a rather unique feature. This effect might be related to the pulse length of 1 ns which allows still ripples formation, but also enables significant debris redeposition. The analysis

of the samples composition and morphology demonstrates that oxide layers and nanostructures, including nanoparticles and LIPSS, can be found on the treated surface areas, which contribute all to such a combined colorization effect. For processing with optimized laser fluence, the hatching distance is the only parameter for the determination of accumulated fluence for oxide-layer color formation. This simultaneously formed structural and nonstructural colors can offer extended opportunities for selectively coloring of metal surfaces for different applications.

References

1. L. Baufay, F.A. Houle, R.J. Wilson, J. Appl. Phys. **61**, 4640 (1987)
2. A.P. del Pino, P. Serra, J.L. Morenza, Appl. Surf. Sci. **197**, 887 (2002)
3. H. Lochbihler, Opt. Express **17**, 12189 (2009)
4. B. Dusser, Z. Sagan, H. Soder et al., Opt. Express **18**, 2913 (2010)

5. V. Veiko, G. Odintsova, E. Ageev et al., Opt. Express **22**, 24342 (2014)
6. P.X. Fan, M.L. Zhong, L. Li et al., J. Appl. Phys. **115**, 13 (2014)
7. A.J. Antonczak, D. Kocon, M. Nowak et al., Appl. Surf. Sci. **264**, 229 (2013)
8. J.M. Guay, A.C. Lesina, G. Cote et al., Nat. Commun. **8**, 12 (2017)
9. A.J. Antonczak, B. Stepak, P.E. Koziol et al., Appl. Phys. A **115**, 1003 (2014)
10. Z.L. Li, H.Y. Zheng, K.M. Teh et al., Appl. Surf. Sci. **256**, 1582 (2009)
11. M. Wautelet, Appl. Phys. A **50**, 131 (1990)
12. J.C. Wang, C.L. Guo, J. Appl. Phys. **102**, 5 (2007)
13. J.C. Wang, C.L. Guo, Appl. Phys. Lett. **87**, 3 (2005)
14. A.Y. Vorobyev, C. Guo, Appl. Phys. Lett. **92**, 041914 (2008)
15. M.S. Ahsan, F. Ahmed, Y.G. Kim et al., Appl. Surf. Sci. **257**, 7771 (2011)
16. J.E. Sipe, J.F. Young, J.S. Preston et al., Phys. Rev. B **27**, 1141 (1983)
17. J. Bonse, S. Hoehm, S.V. Kirner et al., IEEE J Sel Top Quantum Electron **23**, 9000615 (2017)
18. M.A. Garcia, J. Phys. D **44**, 20 (2011)
19. S.A. Maier, M.L. Brongersma, P.G. Kik et al., Phys. Rev. B **65**, 4 (2002)
20. F. Garrelie, J.P. Colombier, F. Pigeon et al., Opt. Express **19**, 9035 (2011)
21. Y. Nishijima, L. Rosa, S. Juodkazis, Opt. Express **20**, 11466 (2012)
22. T. Csizmadia, T. Smausz, C. Tapai et al., J. Laser Micro Nanoeng. **10**, 110 (2015)
23. T. Smausz, T. Csizmadia, C. Tápai et al., Appl. Surf. Sci. **389**, 1113 (2016)
24. A.P. del Pino, P. Serra, J.L. Morenza, Thin Solid Films **415**, 201 (2002)
25. C. Gellini, F.L. Deepak, M. Muniz-Miranda et al., J. Phys. Chem. C **121**, 3597 (2017)
26. V. Veiko, Y. Karlagina, M. Moskvin et al., Opt. Lasers Eng. **96**, 63 (2017)
27. S. Palanco, S. Marino, M. Gabas et al., Opt. Express **22**, 3991 (2014)
28. V. Dudoitis, V. Ulevicius, G. Raciukaitis et al., Lith. J. Phys. **51**, 248 (2011)
29. D.P. Adams, V.C. Hodges, D.A. Hirschfeld et al., Surf. Coat. Technol. **222**, 1 (2013)
30. Z. Gimbutas, L. Greengard, J. Comput. Phys. **232**, 22 (2013)
31. F. Papoff, B. Hourahine, Opt. Express **19**, 21432 (2011)
32. E.D. Palik, *Handbook of Optical Constants of Solids* (Academic Press, San Diego London Boston, 1998), p. 1096